Article

Numerical Investigation of Laser Beam Welding of Stainless Steel Sheets with a Gap

Michele Buttazzoni [1,†], Constantin Zenz [1,†,*], Andreas Otto [1], Rodrigo Gómez Vázquez [1], Gerhard Liedl [1] and Jorge Luis Arias [2]

[1] Vienna University of Technology, Institute of Production Engineering and Photonic Technologies, Getreidemarkt 9, 1060 Vienna, Austria
[2] AIMEN, Poligono Industrial de Cataboi SUR-PPI-2 (Sector) 2, Parcela 3, E36418 - O Porriño - Pontevedra, Spain
* Correspondence: constantin.zenz@tuwien.ac.at
† These authors contributed equally to this work.

Abstract: Keyhole laser beam welding (LBW) of stainless steel sheets with a gap in between is numerically simulated with a three-dimensional, transient multi-physical model for laser material processing. At first, the model's ability to reproduce experimental results on a relatively coarse computational mesh within reasonable computing time, so as to serve as process optimization tool, is presented. An example of process optimization, where a given set of weld seam quality criteria is fulfilled by iteratively optimizing a secondary laser beam, is shown. The relatively coarse mesh, in combination with a good model calibration to the experimental conditions, allows for sufficiently fast simulations to use this approach for optimization tasks. Finally, using a finer spatial and temporal discretization, the dynamic processes in the vicinity of the keyhole leading to the formation of pores are investigated. The physical phenomena predicted by the simulation are coherent with experimental observations found in literature.

Keywords: laser beam welding; welding with gap; keyhole dynamics; pore formation; multiphysical simulation; CFD; process optimization; mesh refinement

1. Introduction

Keyhole laser beam welding (LBW) has gained importance in many industries, e.g. the automotive or aerospace industry, over the past years. The advantages of LBW cover a high level of precision and speed, reduced distortion and a high potential for process automation [1]. It is difficult to experimentally investigate the many physical phenomena involved in laser beam welding as post-experimental investigations do not provide sufficient information on process dynamics and in-situ observations of the transient behaviour, especially inside the keyhole, are not possible on all desired time- and length scales. Zhang et al. [2] managed to directly observe the keyhole by employing a sandwich construction of stainless steel and a special type of glass, using a high-speed camera. However, such experiments require complex setups and do not allow for the investigation of real industrial specifications. Therefore, the development of models which are capable of accurately predicting the physical phenomena involved in LBW remains important and research is ongoing. Reliable models can then help gain understanding of the driving mechanisms behind the formation of defects such as lack of penetration, formation of humps, pores, end craters, etc.
Models of different levels of complexity have been introduced in the past. Ki et al. [3] developed a model based on the level-set method for solving the multiphase flow problem for which they employed some simplifications in the solution of the flow field. Ye and Chen [4] solved the Navier-Stokes equations for the fluid flow by assuming a fixed, cylindrical keyhole and a flat free surface of the liquid. Noori Rahim Abadi et al. [5] recently used a volume-of-fluid approach within OpenFOAM to investigate the effect of beam shaping on the melt pool behaviour in conduction mode laser

 doi:10.20944/preprints202102.0533.v1

beam welding. While their implementation is similar, in the model presented in section 2.1 a crucial component needed for keyhole laser welding was added by implementing an evaporation model. Panwisawas et al. [6] developed a model for keyhole laser beam welding based on a volume-of-fluid approach by implementing it in OpenFOAM and also taking into account evaporation phenomena. A novel addition to the state of the art is provided in the model in 2.1 by the further distinction between two or more gaseous phases, which is of paramount importance when trying to gain a deeper understanding into the process of pore formation as described in Section 4. Furthermore, commercial software is available for the simulation of laser beam welding, as e.g. used by Zhang et al. [7] for the simulation of keyhole laser beam welding. This however comes with the inconvenience of proprietary source code and the inability to change or add models.

An initial effort for developing a model capable of accurately simulating processes involved in laser assisted manufacturing was made by Geiger et al. [8] and Otto et al. [9] by developing a universal multi-physical laser-material processing model based on the open source C++ toolbox OpenFOAM [10], using the volume-of-fluid method for solving the multiphase flow field. The model has since then been substantially improved at the Institute of Production Engineering and Photonic Technologies at Vienna University of Technology. The solver includes the Navier-Stokes equations and continuity equation, coupled with appropriate models for laser beam propagation, laser-material interaction, phase change, keyhole vapour pressure, surface tension and many more physical phenomena necessary to adequately simulate such complex processes. It is capable of accurately predicting a broad range of laser assisted processes, including LBW, laser cutting, laser ablation using ultra-short laser pulses and many additive manufacturing processes (e.g. laser powder bed fusion, laser cladding, etc.) due to the most recent integration of the Lagrangian library into the solver [11,12].

In the automotive industry, welding of overlapping galvanized steel sheets is a common task. As the boiling temperature of Zn lies well below the melting temperature of steel, the vaporization of Zn at the interface and its venting through the melt pool or keyhole can lead to the formation of various defects, including spatter, blowholes and lack of fusion. Several sophisticated techniques to overcome these problems have been suggested, e.g. cutting a slot along the to-be welded line, generating vent holes in the bottom sheet with a pulsed laser or producing humps on the interface surface. Also, many-pass strategies or slow-speed welding have been shown to mitigate the problem, but all of these techniques are irrelevant for the automotive industry because of increased processing time and complexity. By adding a suitable gap at the sheet interface, a stable process can be achieved, yielding high-quality weld seams [13–15]. On the flip side, the presence of a gap can cause different defects, including underfill, porosity, "False Friends" (misconnections without outside evidence), etc. These problems are inherent to gap welding and are independent from the previously described problem of Zn-evaporation and subsequent spatter formation. The reason for the occurrence of a gap in processes with stainless steel sheets that may not be galvanized is mainly due to thermal deformations and the hereby introduced complexity of achieving perfect contact over the whole weld bead length by designing a reliable clamping system. These scenarios are the motivation behind the study presented here, and also by Drobniak et al. [16]. To better understand and prevent the formation of such defects, the simulation model presented here is used to investigate keyhole laser beam welding of stainless steel sheets with a gap.

Section 2.1 describes the simulation model used to perform the investigations presented here and points out further literature regarding the modeling approach. In Section 2.2, the calibration and validation of the model using results of laser beam welding experiments is presented and discussed. In Section 3, a methodology for process optimization through the use of the simulation model on a computationally inexpensive grid is presented. The process optimization was achieved through the addition of a secondary laser beam, which was iteratively adapted in simulations to achieve a set of quality requirements set on the weld and not previously achieved without the secondary beam. Some of the resulting welds are presented. In Section 4, the model is used, on a finer computational grid, to

 doi:10.20944/preprints202102.0533.v1

investigate the physical phenomena leading to pore formation in LBW of overlapping sheets with an interface gap. In Section 5, a conclusion is drawn and an outlook is provided.

2. Simulation Model

2.1. Description of the Model

The model is based on the open source C++ toolkit OpenFOAM [10], which provides a framework for using the finite-volume method to solve continuum mechanics problems described by partial differential equations. The solver is based on the OpenFOAM-native "multiphaseInterFOAM"-solver, which itself is the n-phase extension of the well-known "interFoam"-solver [17]. It uses the volume-of-fluid method to solve multiphase problems involving an arbitrary number of different phases combined with the possibility of dynamic mesh refinement at run-time. This solver has been extensively modified and extended to make it suitable for the simulation of laser-material processing. An overview of the solver and incorporated models for other types of processes can be found in [12]. The models relevant for the simulation of laser beam welding are briefly explained in the following paragraph.

The propagation of laser beams of arbitrary shape (e.g. ring, rectangular, elliptical) and intensity ditribution (e.g. gaussian, tophat, bessel) is calculated by solving a differential radiative transfer equation [18]. A ray tracing algorithm takes into account multiple reflections, which is crucial in keyhole welding simulations. Incident angle dependent transmission and reflection are modeled according to Fresnel's equations, absorption is calculated via Beer's law. The state- and temperature dependent complex refractive index (consisting of the refractive index n and the extinction coefficient κ) of the material therefore needs to be known to correctly model the absorption of laser power within the material. This index is not only dependent on the material but also on the wavelength of the laser [19] and reliable information in the literature is scarce, especially for high temperature applications. Therefore in many cases an estimation and calibration of this parameter using experimental results is needed.

The amount of laser energy absorbed by the material, resulting from the propagation model described above, is included as a source term in the energy equation. The classical energy equation is split into one equation containing the conductive heat transfer and one transport equation for calculating the convective heat transport. Within each time step, the convective part of the energy equation is solved once the flow field is known. Then, the conductive part is solved, including the absorbed laser power as additional source term. This approach is necessary because of the temperature-dependency of the material's heat conductivity and capacity, which are needed within the conductive part of the energy equation.

Each material with its respective phases involved in the problem, i.e. solid, liquid and vapour, as well as ambient gas (e.g. surrounding air, shielding gas), is treated as a distinct phase in the multiphase solver. Phase changes are modeled as mass transfer between the respective phases via the Clapeyron-equation and an accompanying energy transfer. The thus yielded phase change rates have an influence on the pressure and therefore phase change and calculation of pressure have to be calculated together in an iterative manner.

The movement restriction of the solid material is realized through a porous bed model via Darcy's law [20], where a source term in the momentum equation increases with the fraction of solid material inside a cell, letting the velocity approach zero for a solid phase far from any interface.

The solver is capable of dynamic mesh refinement to decrease computational costs. Initially a coarse hexahedral mesh is used, with the cells' size being in the range of half the gap size. Then, dynamically throughout the simulation, the mesh is refined iteratively depending on the presence of propagating or absorbed laser power, presence of liquid phase and presence of re-solidified phase.

 doi:10.20944/preprints202102.0533.v1

2.2. Model Calibration & Validation

Before using the above described model to simulate the process, some material properties, such as the complex refractive index and values for the surface energy of the material need to be calibrated. Although some data on these properties is available in relevant literature, they are not material constants, but (at least) functions of alloy composition, impurities within the alloy, temperature and (in the case of the refractive index) laser wavelength. The dependency of surface tension on temperature is very sensitive to impurities in the form of surface-active elements, mainly oxygen and sulfur. Therefore, there is a lot of discrepancy in the available experimental measurements [21]. However, surface tension related phenomena such as Marangoni currents are of great importance in weld pool dynamics [22] and therefore a fine-tuning of surface tension data against experimental results is necessary. In the case of the complex refractive index, this property and its temperature-dependence have great influence on the laser-material interaction. Data is available for 304L stainless steel e.g. in reference [23], but only one value is given at melting and boiling temperature, respectively, with no information on temperature-dependency in between. Also, no information is provided as to which phase the values refer, e.g. at the melting point, liquid or solid phase. As this property's influence on the process is high, a validation is necessary. Apart from the aforementioned material properties, discretization schemes used by the solver and the amount interface compression within the volume-of-fluid method need to be appropriately chosen in order to obtain a good fit regarding the experimental data. For this purpose, longitudinal and cross sections of 304L stainless steel sheets welded under the presence of a gap are used. The experimental conditions are listed in Table 1.

Table 1. Conditions of the LBW experiments EX1 and EX2 used for model calibration and validation

Parameter	Unit	EX1	EX2
material	–	AISI304L	AISI304L
sheet thickness	mm	1	1
welding speed	mm/s	100	120
laser power	kW	3.5	4
laser wavelength	nm	1070	1070
laser M^2	–	12.4	12.4
laser defocus	mm	7	7
laser radius on top sheet surface	mm	0.31	0.31
gap width	mm	0.3	0.4

The model is calibrated to reproduce the results of EX1 (cf. Table 1). Another experiment, EX2, is then used to validate the model, to ensure the prevention of a model over-fit to the calibration conditions. In EX2, the gap width, welding speed and laser power were different from those in EX1. To validate the values for the complex refractive index, the simulation should be able to reproduce the penetration depth and general heat input measured in the experiments. To calibrate values for the surface energy of the materials, the shape of the cross sections gained from the experiments should be matched, especially at the weld bead top and at the interface, where capillary forces play an important role. The final values for surface energy as a function of temperature and phase are plotted in Figure 1.

Preprints (www.preprints.org) | NOT PEER-REVIEWED | Posted: 23 February 2021 doi:10.20944/preprints202102.0533.v1

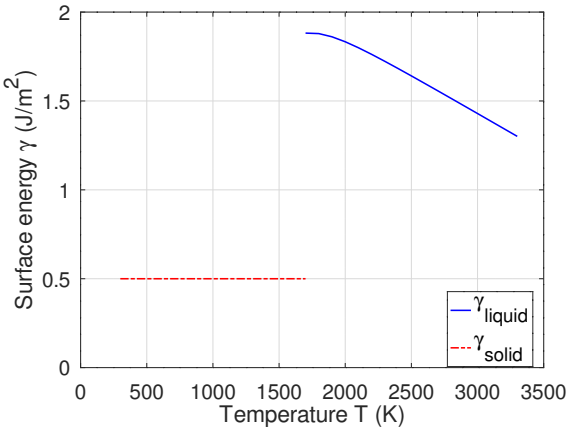

Figure 1. Surface energy γ of solid and liquid phase as function of temperature

Figure 2 and Figure 3 show the comparison of experimental longitudinal and cross sections of EX1 and EX2 and the corresponding simulations S1 and S2 (using the fully calibrated model), respectively. Both the penetration depth over most of the longitudinal section and the cross-sectional weld bead shape are in qualitative and reasonable quantitative agreement. Notably, the defect at the end of the weld bead in EX2 (right end of top longitudinal section in Figure 3), which resembles an end crater, because of the lack of material, resulting in an unfilled keyhole, is reproduced in simulation S2. While in S2 (cf. Figure 3) the plates are still joined, the defect is clearly visible in terms of a decrease in weld bead height. A similar defect is - to a much smaller extent - also visible in EX1 (cf. Figure 2).

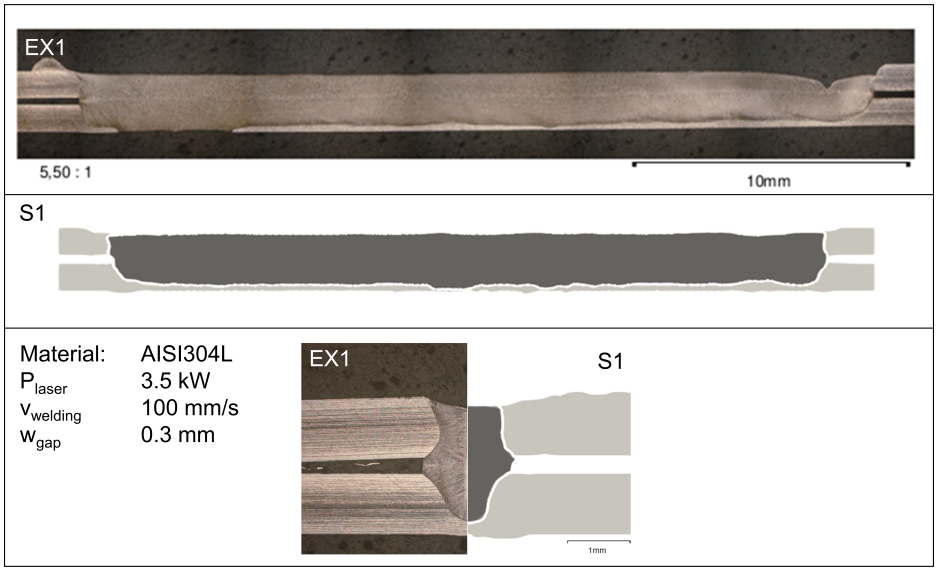

Figure 2. Comparison of experiment EX1 and simulation S1 (model calibration)

Preprints (www.preprints.org) | NOT PEER-REVIEWED | Posted: 23 February 2021 doi:10.20944/preprints202102.0533.v1

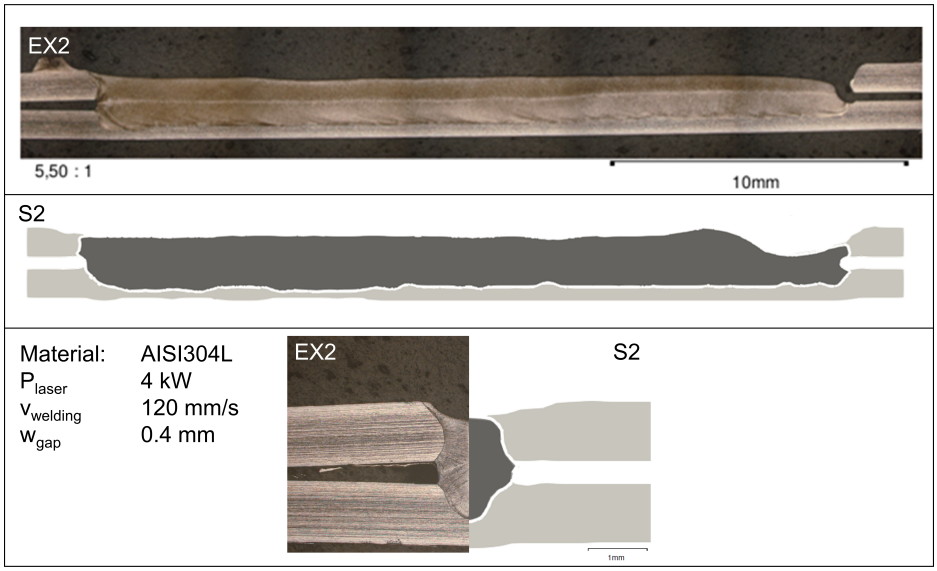

Figure 3. Comparison of experiment EX2 and simulation S2 (model validation)

2.3. Discussion on mesh density

In general, the mesh used for the spatial discretization of the computational domain should be dense enough, i.e. the cell size being sufficiently small, to reach a mesh-independent solution. The temporal discretization during the solution procedure is determined by the Courant-Friedrichs-Lewy number, CFL, which is defined as

$$CFL = \frac{u\Delta t}{\Delta x}, \tag{1}$$

where u is the maximum velocity, Δt denotes the time step and Δx denotes the smallest cell length. By choosing Δt in such a way, that $CFL < 1$, it is ensured that the fluid does not skip a computational cell during the advancement of one time step. It is then clear, that a reduction in cell size by a factor of 2 does not only increase the number of cells by a factor 8 (due to the underlying octree data structure), but also leads to a forced increase in temporal resolution by a factor of 2 in the whole simulation domain. Therefore, a reduction in cell size has great influence on the computational cost of a simulation.

For above mentioned reasons the model was carefully calibrated with the aim of reproducing experimental results in a timely manner so as to be able to use it for optimizing process parameters. During the optimization process, a great number of simulation runs had to be completed within a reasonable amount of time. Therefore, a mesh density was chosen that was sufficient for producing accurate results on a larger scale needed for gaining information about the weld bead shape, as this was the main criterion for the optimization process. It was noted that the cell size was not small enough to resolve many smaller scale effects such as the dynamic waves formation occurring at leading wall of the keyhole.

Within the scope of this paper, the simulation model was used to optimize results of LBW processes on one hand (cf. Section 3) and to investigate highly dynamic small scale processes on the other hand (cf. Section 4). For the latter the finite volume density was dynamically increased by a factor of 8 in the vicinity of the keyhole. This however increased the penetration depth and showed, that it has been underestimated by the coarser mesh.

One of the possible reasons for the increase in penetration when decreasing the cell size stems from the fact that the resolution of surface waves at the keyhole front slightly change the local angle of incidence of the incoming laser beam, which has a great influence on absorption. The wave structures on the keyhole wall resolved by using a sufficiently fine computational grid, can be seen in Figure 4.

Preprints (www.preprints.org) | NOT PEER-REVIEWED | Posted: 23 February 2021 doi:10.20944/preprints202102.0533.v1

It is clear, that with increasing grid coarseness, smaller waves tend to be filtered out and only larger wave structures can be resolved.

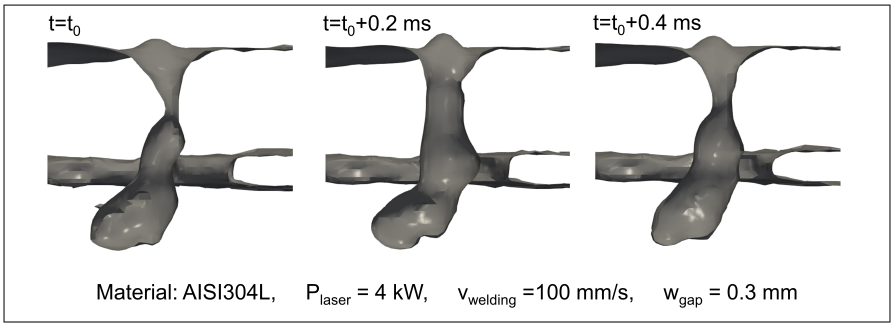

Figure 4. Surface wave structures on keyhole wall on a mesh where the characteristic cell length is roughly equal to $1/8 \cdot w_{gap}$

The effect of laser energy absorption being sensitive to the local incident angle can be seen when plotting the absorption of laser radiation according to the Fresnel equations, which are also discussed by Beyer [19],

$$A_S = 1 - \frac{a^2 + b^2 - 2a \cdot \cos\alpha + \cos^2\alpha}{a^2 + b^2 + 2a \cdot \cos\alpha + \cos^2\alpha}, \tag{2}$$

$$A_P = 1 - \frac{a^2 + b^2 - 2\left(a\left(n^2 - \kappa^2\right) + 2bn\kappa\right)\cos\alpha + \left(n^2 + \kappa^2\right)^2\cos^2\alpha}{a^2 + b^2 + 2\left(a\left(n^2 - \kappa^2\right) + 2bn\kappa\right)\cos\alpha + \left(n^2 + \kappa^2\right)^2\cos^2\alpha}, \tag{3}$$

$$a^2 = \frac{1}{2}\left(\sqrt{\left(n^2 - \kappa^2 - \sin^2\alpha\right) + 4n^2\kappa^2} + n^2 - \kappa^2 - \sin^2\alpha\right), \tag{4}$$

$$b^2 = \frac{1}{2}\left(\sqrt{\left(n^2 - \kappa^2 - \sin^2\alpha\right) + 4n^2\kappa^2} - \left(n^2 - \kappa^2 - \sin^2\alpha\right)\right), \tag{5}$$

$$A = \frac{A_S + A_P}{2}, \tag{6}$$

as function of the angle of incidence, as can be seen in Figure 5. Here, the incident angle α is the angle between the laser beam direction and the surface normal, therefore $\alpha = 90°$ corresponds to a laser beam parallel to the surface. A_S,A_P and A denote absorption of radiation of perpendicular, parallel and no polarisation, respectively. It is obvious that a small deviation in incident angle, especially in the regime of high incident angles as typical for keyhole welding, has a significant effect on the fraction of laser power absorbed by the material.

Preprints (www.preprints.org) | NOT PEER-REVIEWED | Posted: 23 February 2021 doi:10.20944/preprints202102.0533.v1

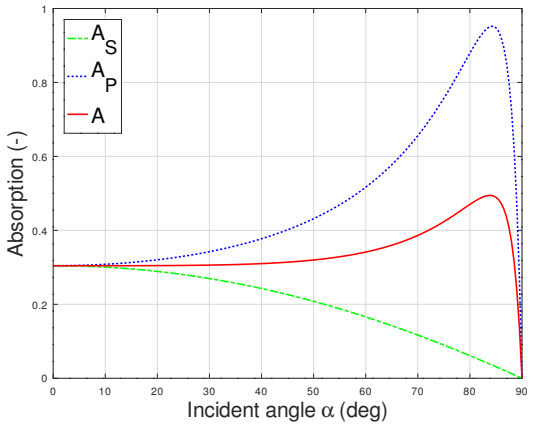

Figure 5. Absorption of laser power by 304L stainless steel at melting point ($n = 9.09$, $\kappa = 4.21$ [23]) as function of incident angle according to Eqs. (2)-(6)

Another consequence of using smaller cells is the decrease in the energy required to reach the melting threshold inside a computational cell, since otherwise the same energy gets distributed over a larger volume. This effect also goes hand in hand with a decrease in numerical diffusion for more refined meshes.
The calibration using the coarser mesh thus yielded values for the complex refractive index (n and κ), as well as a minimum threshold for material in a cell to be taken into account for the absorption of laser energy and a maximum number of reflections being considered by the ray tracing algorithm, which compensated the effects described above. When switching to a finer mesh, these parameters therefore would require a new calibration in order to produce results that are in agreement with the experiments. This is omitted due to the associated high computational cost, as the purpose of the simulations conducted using a finer mesh is not the reproduction of experiments or the use of data to adjust a real-world process, but the investigation of transient effects for the purpose of fundamental research.

3. Beam shape optimization

Using a sufficiently coarse mesh is a possibility to reduce computational cost and thus get faster results, which is of paramount importance when applying any CFD model to a real world application scenario and using it for optimizing many process parameters. To avoid unphysical results due to the coarseness of the mesh, a careful calibration and validation have been performed (cf. Section 2.2).
In the course of the CUSTODIAN project a methodology was developed to increase the quality of a welded seam proposed by an industry partner. The quality requirements set for the welded seams are summarized in Table 2 and schematically illustrated in Figure 6.
In this section, an optimization approach is presented, where the addition of a secondary beam and its effect on the final weld bead geometry is studied. Starting point was an elliptical beam that covered the whole of the melt pool with the aim of introducing more energy and thus fixing some of the issues. In the course of the project, this shape was changed to a rectangular shape due to its easier technical feasibility within the chosen beam shaping approach. Different energy distributions, sizes and positions relative to the primary beam have been tested using the simulation model to iteratively find the optimal beam shape for each experimental condition. The final improvements were reached through the use of a secondary beam with the aforementioned rectangular shape with varying parameters for width, length and power density, depending on the experimental conditions. As post-heating did not seem to be strongly correlated with the resulting weld bead geometry, the secondary beam was shifted, so that the optical axis of the primary beam coincides with the tailing edge of the secondary beam, while maintaining symmetry transversely to the scan direction.

Preprints (www.preprints.org) | NOT PEER-REVIEWED | Posted: 23 February 2021 doi:10.20944/preprints202102.0533.v1

Table 2. Weld quality requirements as defined by the industry partner

Parameter	Value range	reference in Figure 6
total penetration	> 50% of bead length	-
min. weld width at interface	> 0.67mm	(a)
lack of penetration	< 0.2mm	(b)
incompletely filled groove	< 0.2mm	(c)
excessive penetration	< 0.4mm	(d)
excess weld metal	< 0.4mm	(e)
undercut	< 0.1mm	(f)
root concavity	< 0.2mm	(g)

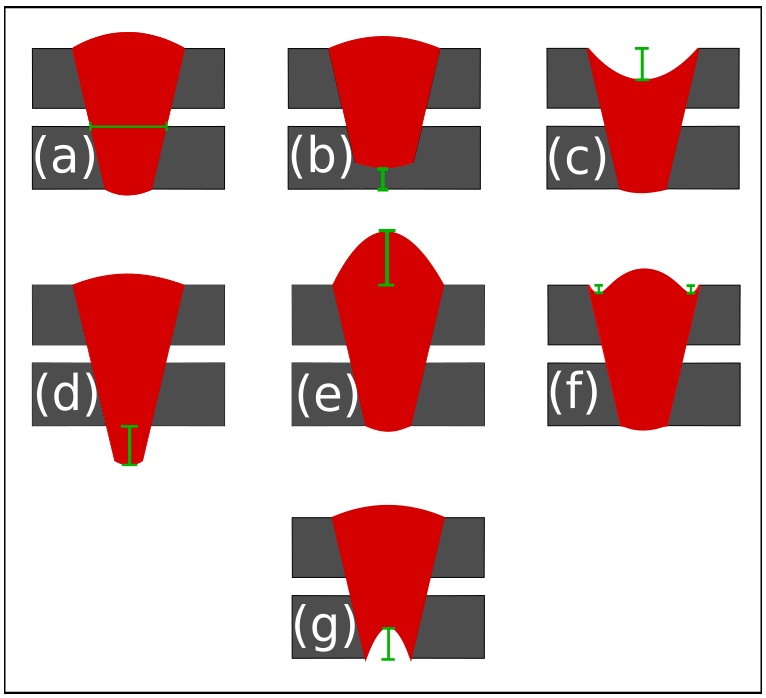

Figure 6. Quality requirements as described in Table 2

For the purpose of improving the weld bead quality, transient effects on very small scales were neglected and thus the coarse mesh previously adopted in the calibration was employed here. It was possible to simulate a process like the ones described in section 2.2 including an optimized secondary beam in under 12 hours on an off-the-shelf AMD Ryzen 7 2700 8 core processor. This allows for testing of many different secondary beam shapes and sizes in differing conditions, varying scan speed, laser power and gap widths, in a fairly short amount of time.

Different parameter combinations of the secondary beam have been found within given technological restrictions, which improved the results of every tested scenario so much as to meet all of the quality requirements given in Table 2. To optimize the beam size it was found that different parameters of the secondary beam had effects on certain aspects of the final weld bead. For example, focusing most of the available secondary beam power onto a "slit" in front of the primary welding beam improved the penetration depth, while widening the beam, decreased the amount of incompletely filled groove seen in the cross sections. Finally the offset (i.e. distance between primary and secondary beam center in welding direction) was set to half the length of the secondary rectangular beam in scan direction, so that its rear edge (considering the weld direction to be forward-facing) coincides with the center of the primary working beam and thus only applies preheating. No substantial positive influence was found when altering this value and no offset in the direction orthogonal to the weld was tested due to symmetry.

Preprints (www.preprints.org) | NOT PEER-REVIEWED | Posted: 23 February 2021 doi:10.20944/preprints202102.0533.v1

In Figure 7, the result of simulation S2-opt is shown, where an optimized secondary laser beam was added to the conditions of EX2 to reach the quality requirements listed in Table 2. Three exemplary cross sections and the longitudinal section from the simulation are given, together with the experimental cross section that was already partly depicted in Figure 3, now with measurements being provided to quantify the improvements through the use of a secondary beam in terms of achieving the quantitative quality requirements on the weld bead. Figure 8 and Figure 9 analogously show the results with an optimized secondary beam for different experimental conditions, where all experimental parameters, that are not explicitly given within the Figures, can be found in Table 1.

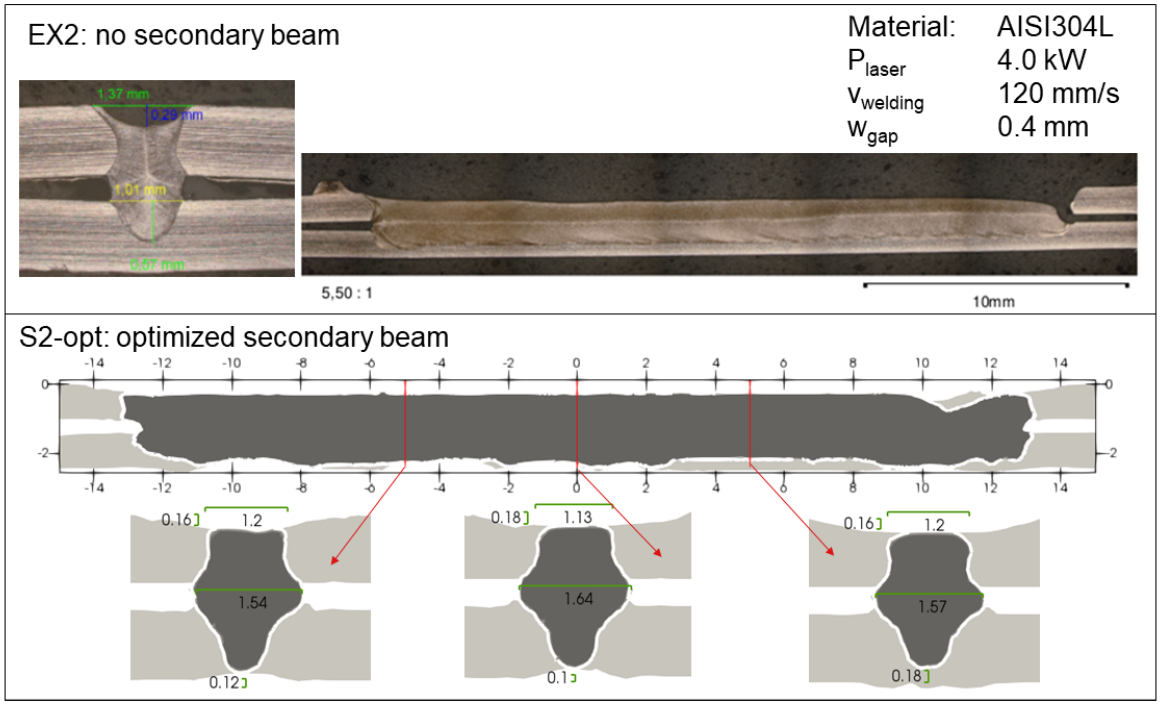

Figure 7. Results of simulation S2-opt, where a secondary laser beam was added to the conditions of EX2 and iteratively optimized. All measurements in (mm).

Preprints (www.preprints.org) | NOT PEER-REVIEWED | Posted: 23 February 2021 doi:10.20944/preprints202102.0533.v1

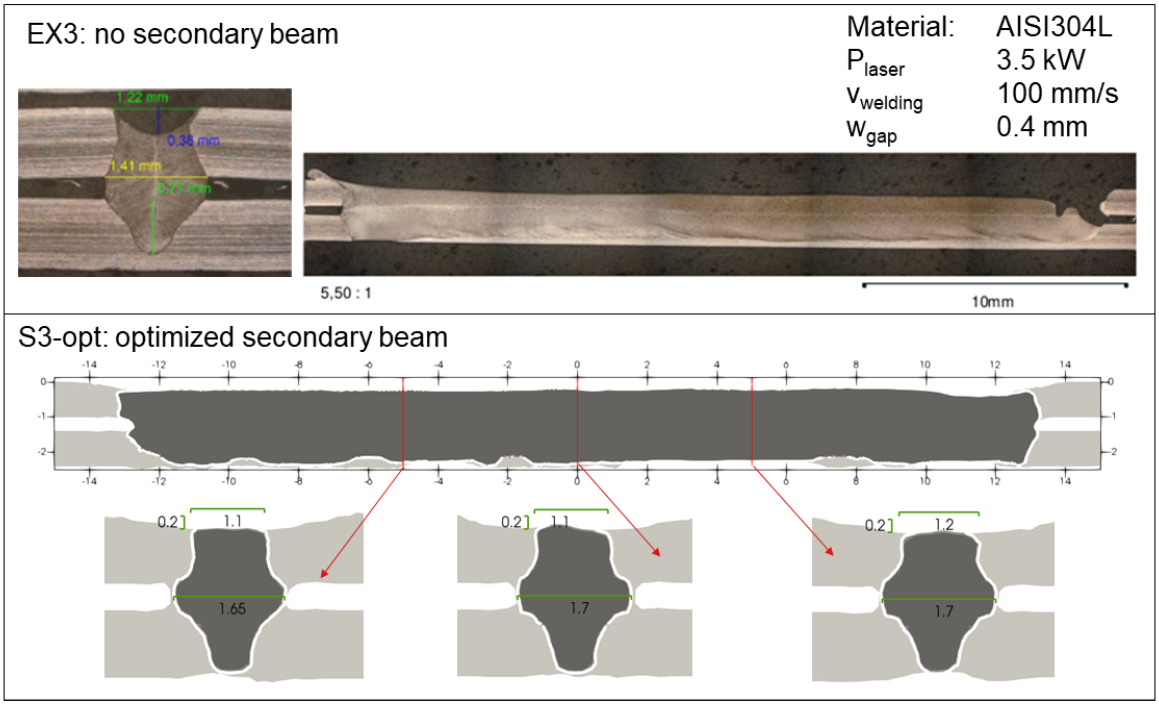

Figure 8. Longitudinal and cross sections of simulation S3-opt, where a secondary laser beam was added to the conditions of EX3 and iteratively optimized. All measurements in (mm).

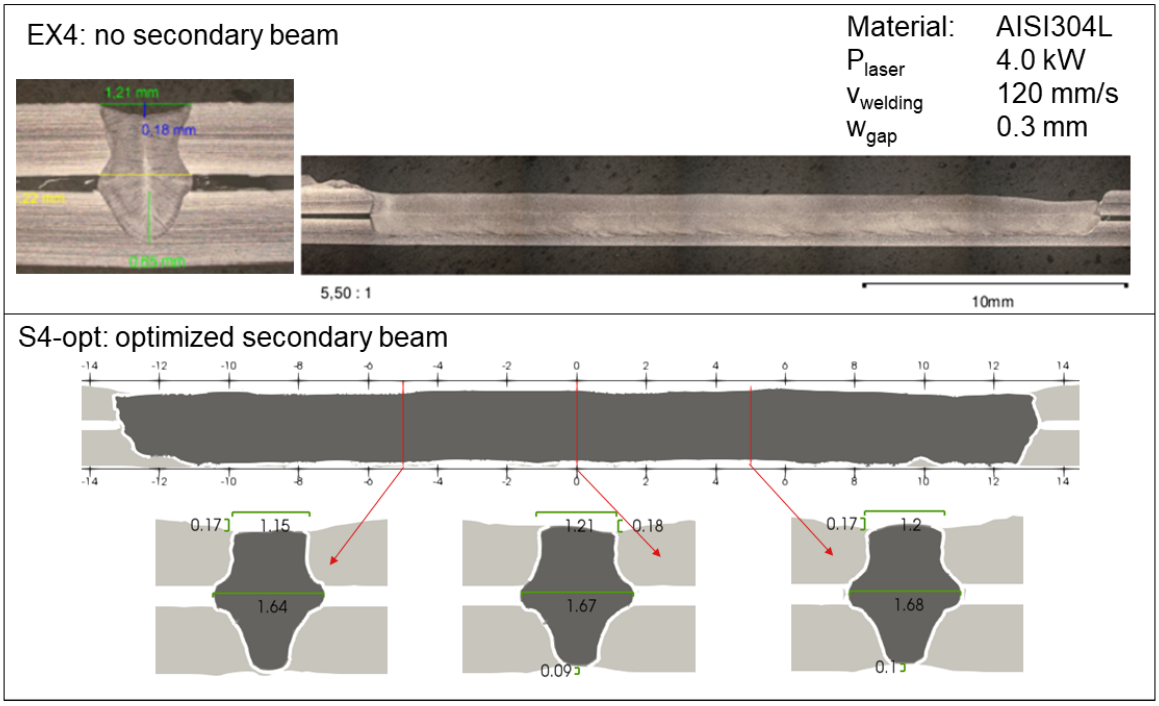

Figure 9. Longitudinal and cross sections of simulation S4-opt, where a secondary laser beam was added to the conditions of EX4 and iteratively optimized. All measurements in (mm).

Details about the final secondary beam parameters used to fulfill all quality requirements are summarized in Table 3.

 doi:10.20944/preprints202102.0533.v1

Table 3. Optimal secondary beam parameters

Simulation	Width(mm)	Length(mm)	Power(W)
S2-opt	1.3	1.5	950
S3-opt	2.2	1.3	1000
S4-opt	1.1	1.5	930

The methodology presented here - using a well-calibrated, three-dimensional and transient CFD model to optimize a multidimensional field of industry-scale LBW process parameters - proves to be computationally affordable and helpful for process design.

4. Keyhole Dynamics and Pore Formation

An interesting effect was observed in systematic simulations of various gap sizes. While in the available experimental longitudinal sections EX1 and EX2 and corresponding simulations S1 and S2 there is no evidence of porosity, when increasing the gap width there is a small range of gap widths, depending on surface tension forces and exact welding geometries, at which the formation of pores can be observed, where the underlying process seems to be strongly linked to the penetration depth and the opening of the front keyhole wall towards the gap. When a pore is formed, the process leading to its formation is similar to the one described by Berger et al. [24], where pore formation processes were experimentally observed by using a CO2 laser and transparent materials (water and ice). In [24], two different types of gas bubbles were observed to appear, where those containing material vapour disappeared quickly, most likely due to full condensation of said vapour. Another type of long-lasting bubbles did not show signs of condensation and it was therefore assumed that those were made up of ambient air. It was also observed that even during a stable process, a bubble can be formed due to a rapid change in absorption because of a change in keyhole geometry, followed by increased evaporation. When a thus formed bubble separates from the capillary, it becomes smaller and remains present to form a pore, with the size depending on the amount of ambient gas trapped inside. It is suggested in [24], that the ambient gas is sucked into the keyhole due to the low pressure at the lower end of the keyhole. As will be shown below, in welding with a gap, the presence of the gap can, for large gaps, lead to the keyhole opening (as e.g. shown in [8]) and promoting the intake of ambient gas even further.

The parameters used for simulation S5, which is used for the discussion of pore formation below, are provided in Table 4. A series of longitudinal sections obtained with simulation S5 is provided, with the respective timestamps of the frames, in Figure 10.

Table 4. Conditions of the LBW simulation S5 used for the investigation of the pore formation mechanism

Parameter	Unit	S5
material	–	AISI304L
sheet thickness	mm	1
welding speed	mm/s	120
laser power	kW	4
laser wavelength	nm	1070
laser M^2	–	12.4
laser defocus	mm	7
laser radius on top sheet surface	mm	0.31
gap width	mm	0.45

The process of pore formation in keyhole laser beam welding starts with a narrow and straight keyhole geometry (Figure 10a). Due to instabilities in the balance of capillary forces and recoil pressure from evaporated metal, caused by the rapidly changing geometry at the locations of inbound laser

Preprints (www.preprints.org) | NOT PEER-REVIEWED | Posted: 23 February 2021 doi:10.20944/preprints202102.0533.v1

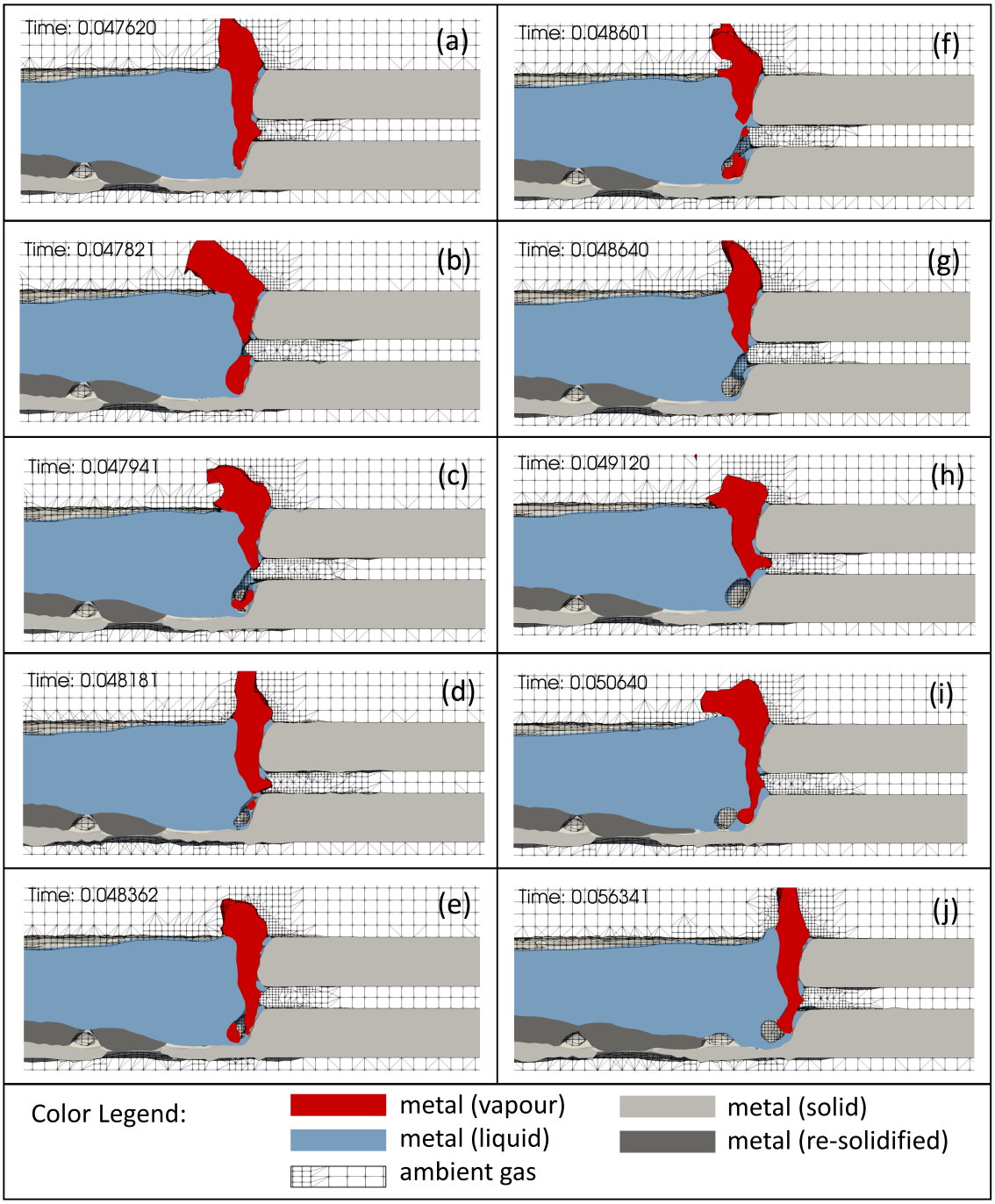

Figure 10. Series of longitudinal sections of LBW simulation S5 illustrating the mechanism leading to pore formation in overlap welding with a gap; simulation time given in seconds

 doi:10.20944/preprints202102.0533.v1

light, a bulge starts to form extending into the liquid. As a consequence of fast evaporation and the resulting shear stresses at the liquid-vapour-interface, upwards-traveling waves form within the melt. These waves, when their amplitude reaches sufficiently high peaks, can block some laser light from reaching the bottom of the keyhole and thus condensation occurs in the deepest region of the keyhole, resulting in low pressure pulling in air from the gap between the plates (Figure 10b). Subsequent low pressure areas form due to further condensation in the region of the lower plate and thus more ambient gas is sucked in (Figure 10c). The remaining vapour in the cavity at the bottom of the keyhole in Figure 10c fully condensates. After about 0.25 ms, liquid has filled the lower part of the gap sufficiently for the absorption at the front wall, and thus evaporation, to increase again. The expanding vapour pushes the now trapped ambient gas further down and towards the back of the keyhole (Figure 10d). Fast moving vapour and constantly changing absorption conditions lead to mixing of the evaporated metal and the trapped gas (Figure 10e) and to the formation of a larger bulge. Approximately 0.25 ms later, a larger liquid melt wave in the upper region of the keyhole constricts the opening entirely and thus blocks laser energy from reaching the bulge in the lower plate. This causes fast condensation in the whole region of the gap and the lower plate where metal vapour was present (Figure 10f) and thus much more air is pulled inwards. Again, increasing evaporation at the front of the keyhole traps the ambient gas, creating a cavity at the bottom (Figure 10g). When closing forces due to surface tension become larger than the vapour pressure holding the keyhole open, it constricts, forming a pore (Figure 10h). If said pore is not formed far enough, or shed with enough momentum, behind the location of the optical axis, it is quickly rejoined with the keyhole and the processes described above repeat. When the pore is large enough and detaches far enough behind the current laser position, it remains stable inside the melt pool, being subject to oscillations due to changes in flow conditions and buoyancy forces (Figure 10i). After some time the whole process starts again with a possible new pore, while the previous pore has settled in its final position (Figure 10j).

In welding processes, the requirement to have full penetration through both plates to be welded helps the ambient gas trapped inside the pores to escape at the bottom of the lower plate. Therefore, pore formation through hereby described processes is only possible when full penetration is not achieved in all parts of the weld bead length. As seen in Figure 10j), pores are only present where full penetration is not achieved. Increasing the power further would change the dynamics inside the keyhole leading to a mostly open keyhole at the bottom of the lower plate and disrupt the fine balance described above so as to hinder pore formation entirely.

5. Conclusion And Outlook

The calibrated and subsequently validated model for keyhole laser beam welding presented in this paper shows its ability to accurately predict weld bead geometries in a timely manner without the use of an unreasonable amount of computational resources, thus making it a great numerical tool for industrial application in process investigation, optimization and data collection. Subsequent refinement and investment of more resources leads to feasibility of using the model for basic research about physical mechanisms inside the material, which are difficult to observe experimentally. Furthermore its generic programming and the lack of process-specific assumptions allows for quick adaptability and the use of a single model to simulate different processes (such as laser ablation, laser scribing, laser drilling, laser-based additive manufacturing, etc.), some of which have already been simulated successfully.

In future scientific efforts an interesting work could be carried out in comparing the found mechanisms of pore formation to experimental data and also investigate the wave generation and propagation inside the liquid material more in depth. A further comparative study between the hereby predicted optimal beam shapes and real-world application will be a product of the CUSTODIAN project.

Author Contributions: conceptualization, M.B., A.O. and C.Z.; methodology, A.O. and R.G.V.; software, M.B., A.O., R.G.V. and C.Z..; validation, M.B. and C.Z.; formal analysis, J.L.A., M.B. and C.Z.; investigation, J.L.A., M.B. and C.Z.; resources, J.L.A., G.L., A.O. and R.G.V.; data curation, J.L.A., M.B. and C.Z..; writing–original draft

 doi:10.20944/preprints202102.0533.v1

preparation, M.B. and C.Z.; writing–review and editing, J.L.A., G.L., A.O. and R.G.V.; visualization, M.B. and C.Z.; supervision, A.O. and G.L.; project administration, A.O.; funding acquisition, A.O.

Funding: This project has received funding from the European Union's Horizon 2020 research and innovation programme under grant agreement nº 825103. CUSTODIAN project is an initiative of the Photonics Public Private Partnership.

Figure 11. EU emblem and Photonics21 logo

Conflicts of Interest: The authors declare no conflict of interest. The funders had no role in the design of the study; in the collection, analyses, or interpretation of data; in the writing of the manuscript, or in the decision to publish the results.

References

1. Katayama, S.; Kawahito, Y.; Mizutani, M. Latest progress in performance and understanding of laser welding. *Physics Procedia* **2012**, *39*, 8–16; DOI:10.1016/j.phpro.2012.10.008.
2. Zhang, M.; Chen, G.; Zhou, Y.; Li, S. Direct observation of keyhole characteristics in deep penetration laser welding with a 10 kW fiber laser. *Optics Express* **2013**, *21 (17)*, 19997–20004; DOI:10.1364/OE.21.019997.
3. Ki, H.; Mohanty, P.S.; Mazumder, J. Modeling of high-density laser-material interaction using fast level set method. *J. Phys. D: Appl. Phys.* **2001**, *34 (3)*, 364–372; DOI:10.1088/0022-3727/34/3/320.
4. Ye, X.-H.; Chen, X. Three-dimensional modelling of heat transfer and fluid flow in laser full-penetration welding. *J. Phys. D: Appl. Phys.* **2002**, *35 (10)*, 1049–1056; DOI:10.1088/0022-3727/35/10/313.
5. Noori Rahim Abadi, S.M.A.; Mi, Y.; Sikström, F.; Choquet, I. Influence of Laser Beam Shaping on Melt Pool Thermocapillary Flow. *Proceedings of the 6th World Congress on Mechanical, Chemical an Material Engineering (MCM'20)* **2020**, *HTFF 125*; DOI:10.11159/htff20.125.
6. Panwisawas, C.; Sovani, Y.; Turner, R.P.; Brooks, J.W.; Basoalto, H.C.; Choquet, I. Modelling of thermal fluid dynamics for fusion welding. *Journal of Materials Processing Tech.* **2018**, *252*, 176–182; DOI:10.1016/j.jmatprotec.2017.09.019.
7. Zhang, L.J.; Zhang, J.X.; Gumenyuk, A.; Rethmeier, M.; Na, S.J. Numerical simulation of full penetration laser welding of thick steel plate with high power high brightness laser. *Journal of Materials Processing Technology* **2014**, *214 (8)*, 1710–1720; DOI:10.1016/j.jmatprotec.2014.03.016.
8. Geiger, M.; Leitz, K.H.; Koch, H.; Otto, A. A 3D transient model of keyhole and melt pool dynamics in laser beam welding applied to the joining of zinc coated sheets. *Prod. Eng. Res. Devel.* **2009**, *3 (2)*, 127–136; DOI:10.1007/s11740-008-0148-7.
9. Otto, A.; Schmidt, M. Towards a Universal Numerical Simulation Model for Laser Material Processing. *Physics Procedia* **2010**, *5*, 35–46; DOI:10.1016/j.phpro.2010.08.120.
10. Weller, H.G.; Tabor, G.; Jasak, H.; Fureby, C. A tensorial approach to computational continuum mechanics using object-oriented techniques. *Computers in physics* **1998**, *12 (6)*, 620–631; DOI:10.1063/1.168744.
11. Gómez-Vázquez, R.; Koch, H.M.; Otto, A. Multi-Physical Simulation of Laser Welding. *Physics Procedia* **2014**, *56*, 1334–1342; DOI:10.1016/j.phpro.2014.08.059.
12. Otto, A.; Gómez-Vázquez, R. Fluid dynamical simulation of high speed micro welding. *J. Laser Appl.* **2018**, *30 (3)*, 032411; DOI:10.2351/1.5040652.
13. Fabbro, R.; Coste, F.; Goebels, D.; Kielwasser, M. Study of CW Nd-Yag laser welding of Zn-coated steel sheets. *J. Phys. D: Appl. Phys.* **2006**, *39 (2)*, 401–409; DOI:10.1088/0022-3727/39/2/024.
14. Mei, L.; Chen, G.; Yan, D.; Xie, D.; Ge, X.; Zhang, M. Impact of inter-sheet gaps on laser overlap welding performance for galvanised steel. *Journal of Materials Processing Technology* **2015**, *226*, 157–168; DOI:10.1016/j.jmatprotec.2015.07.020.
15. Mei, L.; Chen, G.; Jin, X.; Zhang, Y.; Wu, Q. Research on laser welding of high-strength galvanized automobile steel sheets. *Optics and Lasers in Engineering* **2009**, *47 (11)*, 1117–1124; DOI:10.1016/j.optlaseng.2009.06.016.

16. Drobniak, P.; Otto, A.; Gómez-Vázquez, R.; Arias, R.M.; Arias, J.L. Simulation of keyhole laser welding of stainless steel plates with a gap. *Procedia CIRP* **2020**, *94*, 731–736; DOI:10.1016/j.procir.2020.09.134.
17. Deshpande, S.S.; Anumolu, L.; Trujillo, M.F. Evaluating the performance of the two-phase flow solver interFoam. *Comput. Sci. Disc.* **2012**, *5*, 014016; DOI:10.1088/1749-4699/5/1/014016.
18. Modest, M.F. *Radiative Heat Transfer*; Academic Press, **2013**.
19. Beyer, E. *Schweißen mit Laser*; Springer: Berlin, Heidelberg, New York, **1995**.
20. Whitaker, S. (1986). Flow in porous media I: A theoretical derivation of Darcy's law. *Transport in Porous Media*; **1986**, *1 (1)*, 3–25; DOI:10.1007/BF01036523.
21. Su, Y.; Mills, K.C.; Dinsdale, A. A model to calculate surface tension of commercial alloys. *Journal of Materials Science*; **2005**, *40 (9)*, 2185–2190; DOI:10.1007/s10853-005-1930-y.
22. Kou, S.; Limmaneevichitr, C.; Wei, P.S. Oscillatory Marangoni Flow: A Fundamental Study by Conduction-Mode Laser Spot Welding. *Welding journal*; **2011**, *90 (12)*, 229–240.
23. De la Rosa-Santana, G.; Alvarez-Chavez, J.A.; Morano-Okuno, H.R.; Morales-Ramirez, A.J.; Uribe, E. Photomechanical Ablation of 304L Stainless Steel, Aluminium Oxide (Al_2O_3) Thin Film, and Pure Silicon. *Optics and Photonics Journal*; **2016**, *6 (10)*, 275–288; DOI:10.4236/opj.2016.610028.
24. Berger, P.; Hügel, H.; Graf, T. Understanding Pore Formation in Laser Beam Welding. *Physics Procedia*; **2011**, *12*, 241–247; DOI:10.1016/j.phpro.2011.03.031.